Controlled Release of Fe_3O_4 Nanoparticles in Encapsulated Microbubbles to Tumor Cells via Sonoporation and Associated Cellular Bioeffects

Fang Yang, Miao Zhang, Wen He, Ping Chen, Xiaowei Cai, Li Yang, Ning Gu, and Junru Wu*

Fe_3O_4 nanoparticles embedded in the shells of encapsulated microbubbles could be used therapeutically as in situ drug-delivery vehicles. Bioeffects on liver tumor cells SMMC-7721 due to the excitation of Fe_3O_4 nanoparticles attached to microbubbles generated by ultrasound (US) are studied in an in vitro setting. The corresponding release phenomenon of Fe_3O_4 nanoparticles from the shells of the microbubbles into the cells via sonoporation and related phenomena, including nanoparticle delivery efficiency, cell trafficking, cell apoptosis, cell cycle, and disturbed flow of intracellular calcium ions during this process, are also studied. Experimental observations show that Fe_3O_4 nanoparticles embedded in the shells of microbubbles can be delivered into the tumor cells; the delivery rate can be controlled by adjusting the acoustic intensity. The living status or behavior of Fe_3O_4-tagged tumor cells can then be noninvasively tracked by magnetic resonance imaging (MRI). It is further demonstrated that the concentration of intracellular Ca^{2+} in situ increases as a result of sonoporation. The elevated Ca^{2+} is found to respond to the disrupted site in the cell membrane generated by sonoporation for the purpose of cell self-resealing. However, the excessive Ca^{2+} accumulation on the membrane results in disruption of cellular Ca^{2+} cycling that may be one of the reasons for the death of the cells at the G1 phase. The results also show that the Fe_3O_4-nanoparticle-embedded microbubbles have a lower effect on cell bioeffects compared with the non-Fe_3O_4-nanoparticle-embedded microbubbles under the same US intensity, which is beneficial for the delivery of nanoparticles and simultaneously maintains the cellular viability.

Dr. F. Yang, M. Zhang, W. He, P. Chen, X. Cai, L. Yang, Prof. N. Gu
Jiangsu Key Laboratory for Biomaterials and Devices
Nanjing, 210009, China
E-mail: guning@seu.edu.cn

Dr. F. Yang, M. Zhang, W. He, P. Chen, X. Cai, L. Yang, Prof. N. Gu
State Key Laboratory of Bioeletronics
Nanjing, 210096, China

Dr. F. Yang, M. Zhang, W. He, P. Chen, X. Cai, L. Yang, Prof. N. Gu
School of Biological Science and Medical Engineering
Southeast University
Nanjing, 210096, China

Prof. J. Wu
Department of Physics
University of Vermont
Burlington, VT 05405, USA

DOI: 10.1002/smll.201002185

1. Introduction

Recently various nanoparticles (NPs) have attracted considerable interest from researchers in many fields, including chemistry, material science, physics, medicine, and microelectronics, due to their unique chemical, physical and biological properties.[1,2] A variety of nanoparticles made of different materials, from organic NPs (liposomes, polymers, carbon nanotubes, fullerenes) to inorganic NPs (quantum dots, iron oxide, gold particulates), have already opened an exciting avenue for applications in biomedical imaging and drug delivery.[3–9] Superparamagnetic iron oxide nanoparticles represent one kind of NP. Several types of iron oxides have been used as magnetic NPs, including Fe_3O_4, α-Fe_2O_3, γ-Fe_2O_3, and β-Fe_2O_3, among which the magnetite and maghemite are particularly popular in biomedical applications due to their

small NANO MICRO

proven biocompatibility with tissue.[10–12] For example, superparamagnetic iron oxide nanoparticles have played a significant role as magnetic resonance imaging (MRI) contrast agents to better differentiate healthy and pathological tissues or organs. Recently, the resolution and contrast of MRI has been improved noticeably as new MR apparatus and its contrast agents have been introduced. In traditional tumor therapy, histological analysis is performed in vitro after performing biopsy; it is invasive and does not reflect a tissue's real-time status. One way to overcome these shortcomings is the use of MRI by tagging magnetic markers to cells.[13–15] Two approaches were utilized in labeling tumor cells. One is to attach magnetic particles to the cell surface; another is to internalize cells by biocompatible modified magnetic particles via fluid-phase endocytosis, receptor-mediated endocytosis, and phagocytosis.[16–18] However, the effectiveness of diagnostics and therapy of cancers are still limited by the toxic side effects exerted on normal tissues and cells because of the low selectivity and delivery efficacy of NPs. Furthermore, cell-defense mechanisms, such as cell-membrane barriers, could make the intracellular delivery of extracellular agents, such as macromolecules and NPs, difficult or even impossible. All of these obstacles challenge us to find a better controlled-release process of NPs.

Intelligent medical delivery systems or devices are emerging to maximize delivery selectivity and efficacy. One approach that has been used is the so-called stimulus-response method; the stimulus triggers include the pH value, temperature-dependent thermal effects, near-infrared light, magnetic fields, and ultrasound. Novel formulations, ranging from particulates and polymer matrixes to micro- or nano-engineered polymeric or polyelectrolytes multilayered microcapsules, have also been employed.[19–21] For example, an encapsulated microbubble (EMB) consisting of a specific gas surrounded by a shell can be fabricated as an effective delivery microdevice and was extensively used as an ultrasound contrast agent and a drug-delivery vehicle.[22,23] Ultrasound (US) assisted by EMBs, due to its noninvasiveness and ability to focus on the target, has been used in biomedical applications for diagnostic imaging and targeted drug delivery.[24,25] For the latter, the ultrasonically excited oscillations of EMBs may increase the permeability of the nearby cell membrane via a process called sonoporation[26] and promote uptake of the extracellular therapeutic compounds.[27,28] Some previous studies have demonstrated that microbubbles can enhance delivery efficiency of therapeutic compounds when subjected to US. Although some bioeffects that have been reported include increased intracellular levels of hydrogen peroxide, influx of calcium ions, and local hyperpolarization of cell membranes, and so on,[29] the exact mechanisms of the interaction between US and cells remains mostly unknown.

With recent development of nanotechnology, it has been shown that it is possible to attach various NPs, such as iron oxide, quantum dots, and gold particles to the microbubbles' shell.[30,31] In this Full Paper, we demonstrate that we can deliver Fe_3O_4 nanoparticles embedded in shells of encapsulated microbubbles into tumor cells under US excitation (frequency: 1 MHz; acoustic intensity: 0.1, 0.5, and 0.75 W cm^{-2}) through a controlled process of sonoporation. We prepared the Fe_3O_4-NP-embedded microbubbles and used them in an in vitro experiment. We also evaluated the delivery efficiency of the NPs. Furthermore, we further investigated and compared the possible associated cellular bioeffects, including cell apoptosis, cell cycle, and changes in intracellular calcium ions levels induced by NP-embedded microbubbles and microbubbles without NP-induced sonoporation during the delivery process under US excitation.

2. Results and Discussion

2.1. Characterization of Fe_3O_4-Nanoparticle-Embedded Microbubbles

The amount of Fe_3O_4 nanoparticles encapsulated in the microbubbles was 86.47 ± 2.3 μg mL^{-1}. The size distribution of microbubbles was in the ≈3–5-μm range (mean diameter = 3.98 μm), as analyzed by using a 90Plus particle-size analyzer (Brookhaven Instrument Corp, USA). The microbubble suspension was diluted to a concentration of ≈1–6 × 10^8 microbubbles mL^{-1} when experimenting. **Figure 1**A and B shows transmission electron microscopy (TEM) images of Fe_3O_4-NP-embedded microbubble structures before and after US exposure (0.5 W cm^{-2}), which reveals the existence of Fe_3O_4 nanoparticles in the shells of the microbubbles and that the microbubbles can be destroyed after US exposure. After sonication, on the one hand, the Fe_3O_4 nanoparticles and gas encapsulated in the microbubbles can be released; on the other hand, the cavitation induced by the implosion of the microbubble can have disruptive effects on cell-membrane-bound structures in the vicinity and allow the Fe_3O_4 nanoparticle to be delivered into the cells.

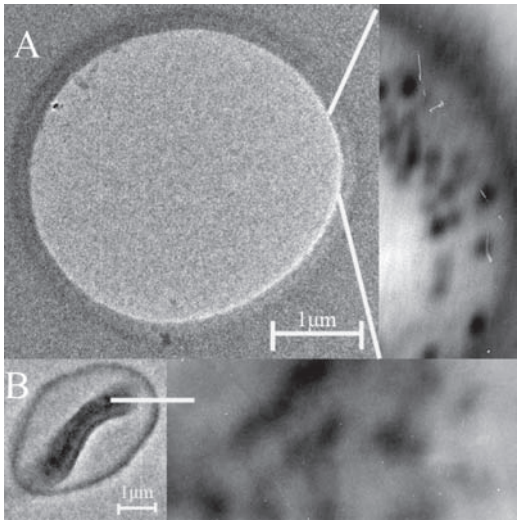

Figure 1. TEM image of Fe_3O_4-nanoparticle-embedded microbubble structures before US exposure (A), which reveals the existence of Fe_3O_4 nanoparticles in the shells of microbubbles. After US exposure (0.5 W cm^{-2}), the microbubbles can be destroyed and the gas and the nanoparticles can be released from the shells (B).

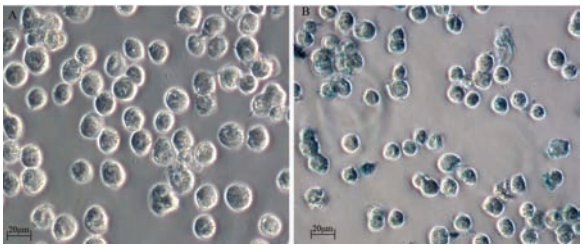

Figure 2. Photomicrography of human liver tumor cells SMMC-7721 treated by US and Fe_3O_4-nanoparticle-embedded microbubbles (B) and without the treatment of US and NP-embedded microbubbles (A). Intracytoplasmic blue particles are clearly visible with Prussian blue staining (×100) after 0.5 W cm^{-2} US exposure for 40 s.

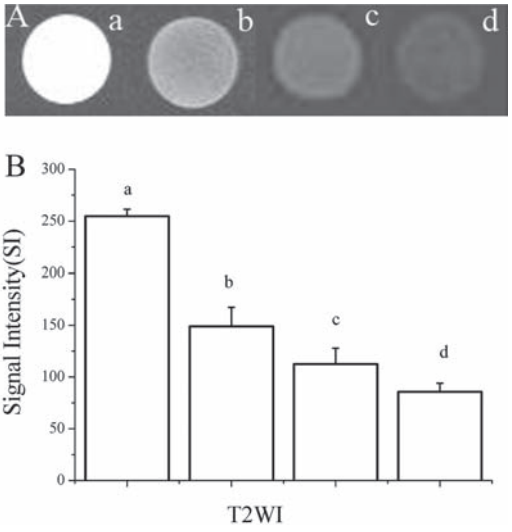

Figure 3. In vitro cell MRI: A) T_2WI of 4 Eppendorf tubes: a) cell solutions without any treatment; cell solution after b) 0.1, c) 0.5, and d) 0.75 W cm^{-2} US and nanoparticle-embedded microbubbles treatments. B) Bar graph showing the mean signal intensity of different cells on T_2WI. There is a significant decrease in the signal intensity of the treated cells in comparison with that of untreated cells.

2.2. Iron-Uptake Efficiency and MR Imaging

After US exposure with Fe_3O_4-NP-embedded microbubbles under intensities of 0.1, 0.5, and 0.75 W cm^{-2}, the quantity of nanoparticles per cell rose from zero to 0.93, 1.19, and 1.57×10^{-6} μg of Fe_3O_4 nanoparticles per cell, respectively. The result shows that there is a significant concentration difference between the US-treated and the control untreated cells. The uptake efficiencies by cells under 0.1, 0.5, and 0.75 W cm^{-2} US and microbubbles exposure are 26.89 ± 3.46, 34.40 ± 2.13, and 45.39 ± 4.66%, respectively. The different delivery efficiencies indicate that the nanoparticles embedded in the microbubbles can be delivered into a tumor cell in a controlled fashion by adjusting the US intensity. **Figure 2**B shows images of the cells stained with Prussian blue. Blue particles could be seen in treated cells after sonication, whereas no blue particles were seen in the control cells without the treatment of US and NP-embedded microbubbles (Figure 2A).

T_2-weighted MR images (T_2WI) after sonication under 0.1, 0.5, and 0.75 W cm^{-2} with NP-embedded microbubbles are shown in **Figure 3**A. Their corresponding signal intensity (SI) is shown in Figure 3B. The T_2WI results demonstrate a significant signal intensity decrease after treatment with US and Fe_3O_4-nanoparticle-embedded microbubbles, which indicates that the Fe_3O_4 nanoparticles efficiently labeled the tumor cells and can be detected by MR imaging. With an increase in the US intensity, the MR imaging becomes darker and darker, which indicates that more Fe_3O_4 nanoparticles are delivered into the cells, just as in the iron-uptake efficiency results.

2.3. Scanning Electron Microscopy (SEM) Morphology

Figure 4 shows SEM images of cells under different US exposure levels. Normally, the morphology of the cells is spherical in shape and their surfaces are relatively smooth (Figure 4A and A-1). Dimple-like craters of various sizes appeared in the membrane surfaces of many cells after US exposure with EMBs during the experiment. Figure 4B–G shows images corresponding to 0.1, 0.5, and 0.75 W cm^{-2} with Fe_3O_4-NP-embedded microbubbles and non-NP-embedded microbubbles (magnification = 5000). The corresponding local enlarged images (magnification = 50 000) are shown in Figure 4B-1 to G-1. Rough regions and small pits started to appear when the acoustic-pressure amplitude increased. After treatment with US and NP-embedded microbubbles, nanoparticles can be seen on the surface or cytoskeleton of the treated cell membrane. Energy-dispersive X-ray analysis (EDXA) results after US exposure with non-NP-embedded and Fe_3O_4-NP-embedded microbubbles are shown in Figure 4H and I, respectively. The results reveal that the cell interaction with Fe_3O_4-NP-embedded microbubbles after US exposure consists of C, N, O, Na, P, S, and Fe elements, which indicate the existence of Fe_3O_4 NPs in the cell structure. The Si peaks in the spectrum come from the silicon substrates. It is interesting to note that when applying the same acoustic intensity, it seems that the non-NP-embedded microbubbles have a bigger influence on the cell cytoskeleton of the cell membrane. This difference in cell-surface morphology indicates that the effects of US on cells were amplified by the EMBs. It also suggests that the controlled-release delivery applications of US are based on its ability to facilitate transport across a membrane surface by increasing their porosity or permeability, which is beneficial to the nanosized particles entering the cell.

2.4. Cell Apoptosis and Cell Cycle

The cells were tested by annexin/propichium iodide (PI) double-stain flow cytometry and the apoptosis results and the viability of cells are shown in **Figure 5**. When the US intensity is high enough, microbubbles may implode due to the inertia of the inrushing fluid (inertial cavitation). As a result, fluid streams and microjets develop that can transiently perforate the membranes of nearby cells and hence enhance

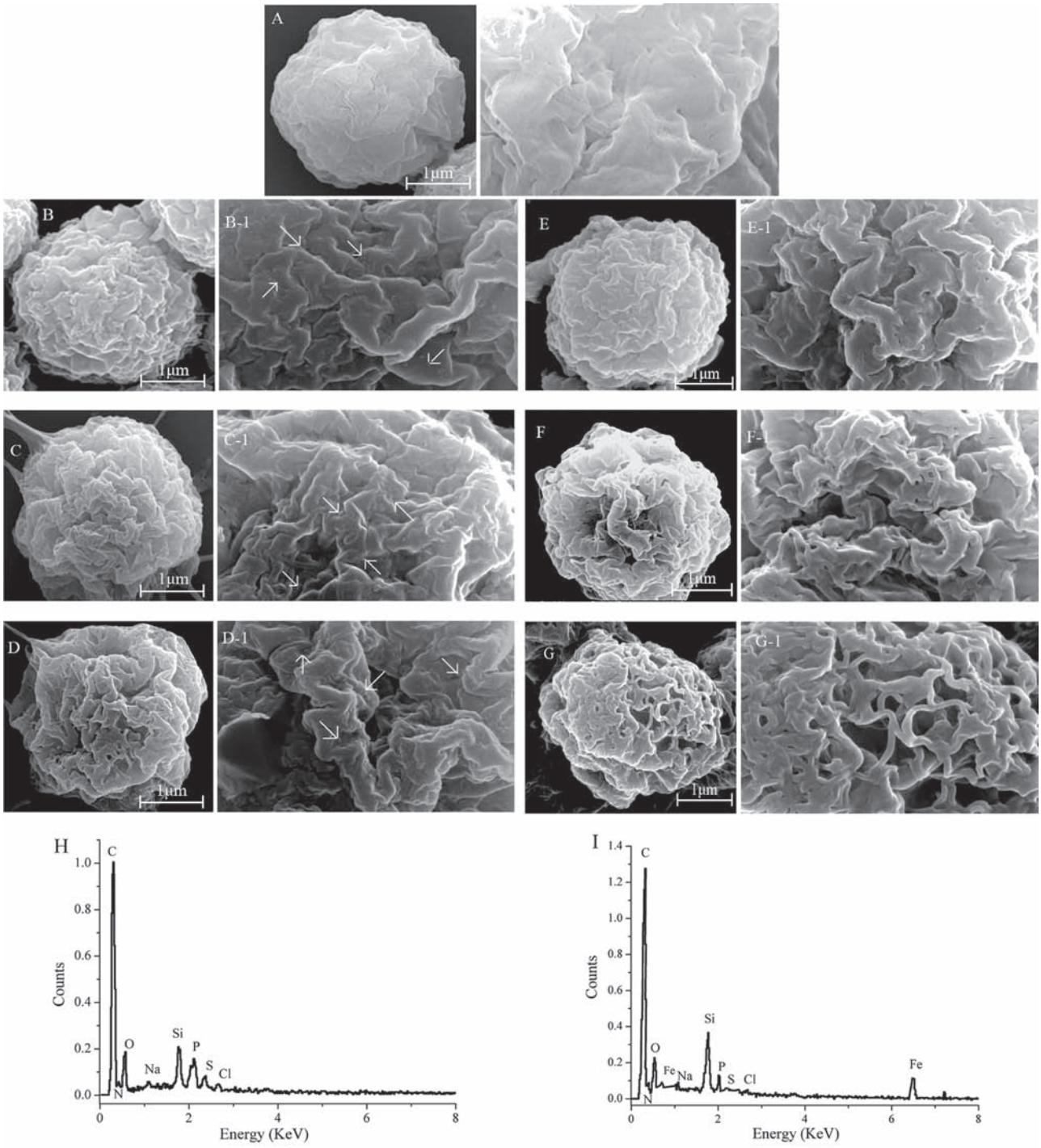

Figure 4. SEM images of 7721 cells irradiated without US exposure in the presence of EMBs (A,A-1). After B,E) 0.1, C,F) 0.5, and D,G) 0.75 W cm^{-2} US exposure for 40 s with Fe_3O_4-NP-embedded microbubbles (B,C,D) and non-NP-embedded microbubbles (E,F,G). The B-1 to G-1 images are local enlarged magnifications of the corresponding group, in which the plasma membrane structure, the cytoskeleton, and the nanoparticles on the membrane (arrows) can all be clearly seen. The EDXA spectra after 0.5 W cm^{-2} US exposure for 40 s with non-NP-embedded and Fe_3O_4-NP-embedded microbubbles are shown in (H) and (I), respectively. The image in (I) clearly reveals that the cell interaction with Fe_3O_4-NP-embedded microbubbles after US exposure consists of Fe elements, except the C, N, O, Na, P, and S elements in image (H), which indicates the existence of Fe_3O_4 NPs in the cell structure.

the intracellular uptake of nanoparticles. However, during this process, the viability of the cells is bound to be affected. Therefore, in order to improve the cellular uptake of external agents, it is important to avoid cellular death. In this experiment, the highest apoptosis efficiency was about 30 and 23% when induced by non-NP-embedded microbubbles and Fe_3O_4

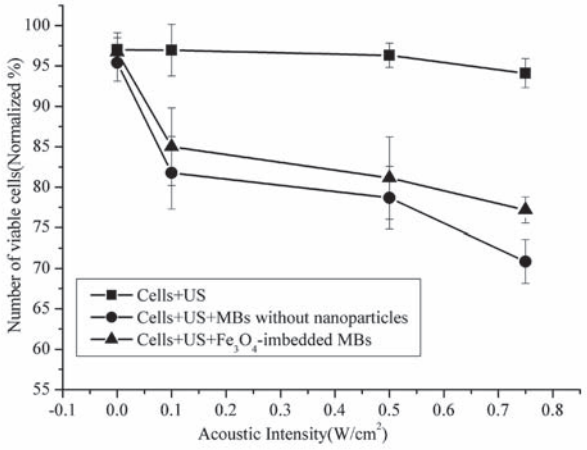

Figure 5. Cell permeability increases and viability decreases with an increase in ultrasound intensity (0.1, 0.5, and 0.75 W cm^{-2}).

NP-embedded microbubbles, respectively, under 0.75 W cm^{-2} (Figure 5) US exposure, which demonstrates that although some tumor cells were killed after US and microbubble treatment, the viability of the whole cells can be maintained. After the nanoparticles entered into the SMMC-7721 cells, the Fe_3O_4 nanoparticles also possessed a suitable cytotoxicity property for biomedical applications.[32] Besides, it seems that the Fe_3O_4-NP-embedded microbubbles preserve the cell viability better, which suggests that Fe_3O_4 NP attached inside the shell may enhance the microbubble stability under excitation by an acoustic field by introducing additional attenuation to the oscillations. Thus, the cavitation energy induced from the Fe_3O_4-NP-embedded microbubbles is smaller than non-NP-embedded microbubbles under the same acoustic intensity, which decreased the destruction of the cells; this result is consistent with the SEM results.

After measuring the cell apoptosis, the cell cycles were also studied by staining with PI and analyzed by fluorescence-activated cell sorter (FACS). The cell numbers in different cell cycles after US and microbubble treatment are shown in **Figure 6**. The results demonstrate that the distribution

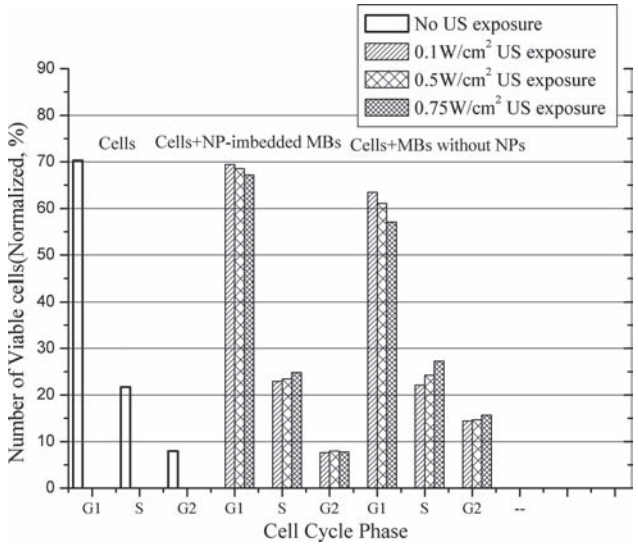

Figure 6. Cell viability exposed to US depends on the cell-cycle phase.

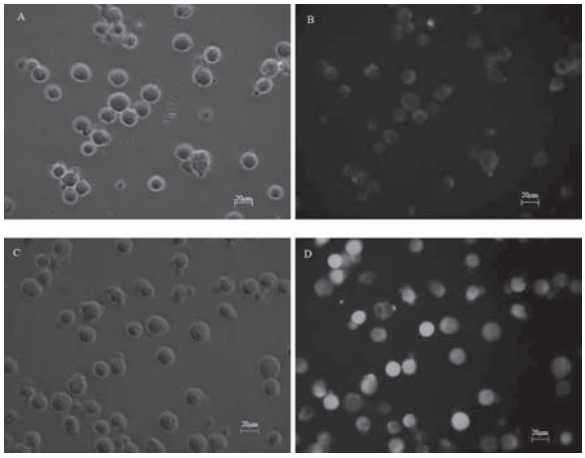

Figure 7. Typical images of SMMC-7721 cells after Fluo-3 staining (×100). A,B) 7721 cells without the US and microbubbles treatment under bright field and epifluorescent field; C,D) 7721 cells after US exposure (0.5 W cm^{-2}) and treatment with nanoparticle-embedded microbubbles under bright field and epifluorescent field.

of viable cells with respect to their cell-cycle phase changes after different acoustic-intensity treatments. For example, in the untreated sample, cell-cycle-dependent viability after handling was 70.29 (G1), 21.71 (S) and 8.00% (G2) (normalized with respect to a total viability of 96.70%). After treatment with 0.1 W cm^{-2} US and NP-embedded microbubbles and non-NP-embedded microbubbles, the cell-cycle dependent viability became 69.42 (G1), 22.96 (S) and 7.62% (G2) (normalized to a total viability of 85.01%) and 63.46 (G1), 22.12 (S) and 14.42% (G2) (normalized to a total viability of 81.79%), respectively, which demonstrates that more cells were killed by ultrasound and microbubble exposure in the G1 phase compared with the S and G2 phases. A similar effect was observed in samples treated at higher acoustic intensity. This may be related to differing cellular viscoelastic properties of the cell membrane that change during the cell cycle after treatment with US and microbubbles. At the same time, the iron-uptake efficiencies by cells under 0.1, 0.5, and 0.75 W cm^{-2} US and NP-embedded microbubbles exposure are 26.89, 34.40, and 45.39%, respectively, which indicates that cells in different phases of their cell cycle showed varied sensitivity to permeabilization when exposed to US with microbubbles. In general, the Fe_3O_4-NP-embedded microbubbles have lower effects on the cell cycle than microbubbles without nanoparticles.

2.5. Calcium Transport During Sonication

Figure 7A–D contain typical photos of 7721 cells dyed by Fluo-3 taken after treatment with US with Fe_3O_4-NP-embedded microbubbles under bright field and epifluorescent field, respectively. The qualitative flow cytometry results are also shown in **Figure 8**. The results of Fluo-3 fluorescent staining demonstrate that with an increase in the acoustic intensity, the non-NP-embedded microbubbles and NP-embedded microbubbles both increase the intracellular Ca^{2+}

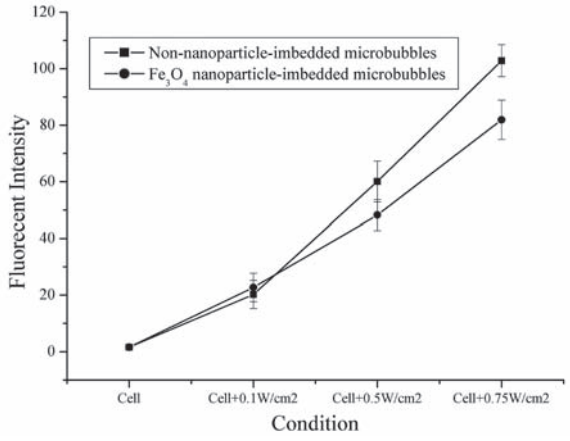

Figure 8. The Fluo-3 fluorescent intensity changes after US (0.1, 0.5, and 0.75 W cm^{-2}) and microbubbles treatments.

concentration. It was found that US alone did not affect cell-membrane permeability for low calcium (2.05 ± 0.34%) concentration, whereas US and microbubbles induced a significant increase in intracellular calcium levels. The Ca^{2+} fluorescent intensity facilitated by the non-NP-embedded microbubbles was higher than the Fe_3O_4-NP-embedded microbubbles.

It has been reported that there is a direct link between a rise in intracellular Ca^{2+} levels, hyperpolarization, and an increased uptake of macromolecules via endocytosis and/or macropinocytosis.[33,34] In particular, intercellular calcium is an important second messenger that regulates signal transduction and other intracellular processes. Changes in the levels of intracellular Ca^{2+} may trigger many cellular processes. In this study, we found that when the US microbubble activated the tumor cells, their Ca^{2+} signals rose because of the spontaneous self-protection response. As a consequence, the increase in intracellular calcium levels after US and microbubble exposure may induce the corresponding subtle cellular bioeffect. First of all, resealing or self-repairing is required by many cells for survival and it was discovered that the ability of a disrupted plasma membrane to reseal itself would be Ca^{2+}-regulated exocytosis. Upon disruption, the consequent Ca^{2+} entry could bring about significant changes in plasma membrane and cytoskeletal architecture.[35] Thus, cytoplasm by itself is capable of erecting a new membrane boundary when challenged with the potentially toxic extracellular environment and Ca^{2+} is the trigger for this response. Cell-membrane disruption generated by shear stress due to oscillating EMBs excited by US might trigger intracellular Ca^{2+} changes[36] and the increased Ca^{2+} entering the disruption area cause vesicles present in cytoplasm under the disruption site to fuse rapidly with one another and also with the adjacent plasma membrane. Once the microscopic pores emerged on the cell membrane during the sonoporation, the elevated Ca^{2+} concentration can be found beneath the disruption site. Next, fusion events triggered by Ca^{2+} simultaneously can erect a membrane boundary, meld plasma, and patch membranes; this is how cells survived from sonoporation.[37–39] That is to say, in order to maintain the viability of the cells after US and microbubbles treatment, the intracellular Ca^{2+} is bound to respond to it. Besides, as shown by the SEM images in Figure 4, relatively larger plasma membrane damage was generated by non-NP-embedded microbubbles than by NP-embedded microbubbles. Thus, more Ca^{2+} is required in order to respond (Figure 8). This may explain why the Fe_3O_4-NP-embedded microbubbles triggered a lower Ca^{2+} increase than the non-NP-embedded microbubbles.

To reseal the disrupted cell membrane, the intracellular triggered Ca^{2+} migrates to the plasma membrane and the disturbed intracellular Ca^{2+} concentration in situ may also induce corresponding subtle bioeffects. In this study, we found that more cells were killed by US and microbubble exposure in G1 phases compared with S and G2 phases (Figure 6). It is well known that Ca^{2+} has an important role throughout the mammalian cell cycle and is especially important in the early G1, G1/S, and G2/M transitions. Cells are most sensitive to depletion of extracellular Ca^{2+} in G1, in which Ca^{2+} is important for the expression of genes.[40,41] Based on the results of cell apoptosis, cell cycles, and intracellular calcium changes, under the same acoustic intensity exposure as the non-NP-embedded microbubbles, the Fe_3O_4-NP-embedded microbubbles can efficiently deliver the Fe_3O_4 nanoparticles into the tumor cells and, at the same time, have minimum impact on normal living cells.

2.6. Nanoparticle-Controlled Release and Its Role in Sonoporation

It was reported that the interaction between the cell and NPs can be enhanced by surface modification of the NPs.[15] The release of nanosize particles in response to a physical or chemical stimulus would be advantageous in order to deliver more efficiently to a specific target. Ultrasonic treatment is one of the approaches for the activated release of the encapsulated materials from the carriers.[42] In this study, the Fe_3O_4 nanoparticles were loaded into the microbubbles to facilitate their uptake by the tumor cells, which could then be tracked by MR imaging. The results demonstrate that it is possible to control the release of Fe_3O_4 nanoparticles from the microbubbles by adjusting the US intensity. This process mainly relies on acoustic cavitation, including the stable (noninertial) and transient (inertial) cavitation. Among other things, stable cavitation generates secondary time-independent flows (acoustic streaming) and transient cavitation leads to the generation of very high local temperatures, pressures, and free radicals that can have disruptive effects on membrane-bound structures in the vicinity.[25] The presence of Fe_3O_4 nanoparticles in the shell of polymer-encapsulated microbubbles decreases the acoustic cavitation effects on the nearby cells, minimizing the destructive effects to a degree, while maintaining uptake of NPs by the cells. This was illustrated by the different cell permeabilities (Figure 4) and cell apoptosis (Figure 5) generated by the non-NP-embedded microbubbles and NP-embedded microbubbles under US excitations with the same acoustic parameters. The reason may be related to the fact that the microbubbles with Fe_3O_4 NPs embedded in their shells cause

an increase in stiffness and attenuation compared to their counterparts without nanoparticles. Hence, the presence of an appropriate amount of Fe_3O_4 nanoparticles, which increase the viscous damping and stiffness of the microbubble shell, may be beneficial for achieving high delivery efficiency with better cell viability. When the MRI-contrast-agent Fe_3O_4 nanoparticles encapsulated in the microbubbles are delivered into the tumor cells under US exposure in a controlled fashion, the migration, proliferation, differentiation, and apoptosis of the tumor cells then can be tracked by MRI continuously and noninvasively.[43,44] Our studies are preliminary and the interaction between the nanoparticles and the cells excited by US needs to be investigated further. For example, the nanoparticles may influence the extracellular matrix, plasma bilayers, and cytoskeletons, which, in turn, may also impact the intra- and intercellular bioeffects.

3. Conclusion

We have demonstrated it is possible to control the release of Fe_3O_4 NPs from shells of embedded microbubbles into cells by ultrasonic excitation. Consequently, those Fe_3O_4-NP-labeled cells can be noninvasively tracked by MRI. Furthermore, the appropriate balance between generation of suitable cell porosity for drug delivery and, simultaneously, maintenance of the integrity of the plasma membrane could be achieved by adjusting the acoustic intensity of the applied US. The method described in this paper may provide medical professionals with an alternative way to deliver nanoparticles into targeted cells noninvasively and effectively. It is noted that the sizes of most biological cells are on the order of 10–100 μm, the microbubbles are on the order of 1–10 μm, and the embedded nanoparticles in the shells of microbubbles are on the order of nanometers. The multiple-scale interactions during sonoporation are rather complicated and warrant further research.

4. Experimental Section

Microbubble Preparation and Cell Culturing: The shells of microbubble samples used in the experiment were polymer either with or without embedded Fe_3O_4 nanoparticles. The Fe_3O_4 NPs (12-nm mean diameter) embedded in their shells were hydrophobic nanoparticles with no surface modification (Jiangsu Laboratory for Biomaterials and Devices). The stable polymer-coated microbubbles (nitrogen filled) were prepared by a double-emulsion solvent-evaporation interfacial deposition process, as described previously.[45] Briefly, first, the poly(DL-lactide) (PLA; Shandong Key Laboratory of Medical Polymer Materials, China) and a Fe_3O_4-NP-coated emulsion was prepared; they were then poured into a polyvinyl alcohol (PVA; 5 w/v%, from Alfa Aesar) solution and mixed mechanically for 2 h to form a stable double-layered emulsion. The resulting suspension was then lyophilized by the freeze-drying method and stored with a tight seal, filled with nitrogen gas. Before mixing with cells, the sterile phosphate buffer solution (PBS; pH 7.4) was added to the sterile lyophilized microbubble samples. The microbubbles without NPs embedded in their shells were prepared in the same way, except that Fe_3O_4 NPs were not included during the preparation process. They used the same shell materials and had a similar mean diameter and concentration of suspension.

SMMC-7721 cells (a human liver carcinoma cell line) were purchased from Shanghai Cellular Institute of China Scientific Academy (Shanghai, China). They were cultured as monolayers in RPMI1640 media and fetal bovine serum (FBS; 10%). They were grown in a humidified CO_2 (5%) atmosphere at 37 °C. For US-exposure experiments, exponentially growing cells were harvested and resuspended in fresh RPMI1640 media with FBS (10%). The concentration of the cells was diluted to a concentration of $\approx 1-6 \times 10^6$ cells mL^{-1}. For each trial, a cell suspension (1 mL) and microbubble solution (0.1 mL) were placed into a plastic tube of 15-mm diameter and 75-mm length (Kimble, Owens-Illinois, Toledo, OH) with a sound-transparent polymer-membrane bottom. The concentration ratio of microbubbles to cells was about 10:1.

Ultrasound Exposure: The ultrasound-exposure system was described in our earlier publication.[37] Briefly, a 1 MHz unfocused 30-mm-diameter single-element transducer (Yu-Chao Electronics Co., Ltd. Wu Xi, China) was positioned in a water tank. The transducer was connected to an arbitrary waveform generator (Agilent 33250A, USA) and a 50 dB broadband radio frequency (RF) power amplifier (ENI 2100L, Rochester, NY, USA). Cells were exposed to sine-wave US tone bursts with 20 cycles per burst at a pulse-repetition frequency (PRF) of 10 kHz. The plastic test tubes of 15-mm diameter and 75-mm length filled with cell and microbubble suspension bottomed by a sound-transparent thin polymer membrane were rotated at 60 rpm by a direct current (DC) motor throughout the exposure period; the rotation helped to mix the microbubbles with the cells evenly and the distance between the bottom of the tube and the transducer was 6 cm. The US spatial and temporal averaged intensities used in the experiments were 0.1, 0.5, and 0.75 W cm^{-2}, as verified with a calibrated hydrophone (TNU0001A, NTR, Seattle, WA, USA). The total exposure time was 40 s.

Measurement of Fe_3O_4-NP Concentration within Cells and Cell MR Imaging: After the US exposure, the cells were separated from microbubbles in suspension by centrifugation (1000 rpm, 8 min, Eppendorf centrifuge 5804R, Brinkmann Instruments, Wesbury, NY, USA) and washed three times with PBS (pH 7.4) at room temperature (20 °C). In order to measure the iron concentration within the cells, the cell suspensions were dissolved in hydrochloric acid (HCl, 37%) for 24 h and analyzed by using an atomic absorption spectrometer (180–80 Hitachi, Japan).[46] Results were expressed in terms of the number of Fe_3O_4 nanoparticles per cell.

After being treated under US exposure, cells were washed with PBS three times to remove excess free microbubbles and their fragments. For MR imaging, the other cells mixed with PBS solution were placed in an Eppendorf tube of 1 cm in diameter. A phantom study was then performed using a 7.0 Tesla Micro-MRI system (PhamaScan, Bruker, Germany). The MRI sequence was a T_2-weighted gradient-echo (620/15.7; flip angle: 35°) sequence. Images were acquired with a matrix size of 256 × 256, section thickness of 2 mm, and field of view (FOV) of 10 mm × 10 mm. The region of interest for signal-intensity (*SI*) measurement was 20 mm^2. The percentage change in *SI* was calculated using the following equation: $\Delta SI = (SI_{US} - SI_{control})/SI_{control} \times 100\%$, where SI_{US} and $SI_{control}$ were the *SI* values of the treated and the untreated cells with US assisted by microbubble exposure, respectively.

Characterization of Cell Morphology After Ultrasound Exposure: After being treated by US exposure, part of the cells were washed

small NANO MICRO

with PBS three times to remove excess free microbubbles and their fragments. For Prussian blue staining, the cells were incubated with potassium ferrocyanide (2%) in HCl (6%), which indicates the cells' profile and intracellular iron particles.

To observe the effects of ultrasound exposure on the cell membrane, 7721 cells for each case were imaged using SEM at a different magnification. After ultrasound exposure, each sample was fixed with glutaraldehyde solution (2.5%) for 1 h at 4 °C and then washed twice in PBS (pH 7.2). Alcohol dehydration followed in 33, 50, 66, 80, 90, and 100% ethanol for 20 min, each stage being repeated twice. Next, critical-point drying was performed using critical-point driers (Emitech K850X, UK) and a field-emission SEM system (FEI Sirion-200, USA) was used with a gun acceleration voltage of 20.0 kV and a working distance of 8 mm. In order to prove the existence of magnetic NPs in cell SEM images, the elements on the cell were characterized by EDXA (FEI XL30, USA).

Cellular Apoptosis and Cell-Cycle Analysis: The cells mixed with microbubbles with and without embedded Fe_3O_4 NPs in their shells were sonicated by US exposure for 40 s. They were then collected from the corresponding groups and washed three times with PBS and resuspended in annexin medium (50 μL). After adding annexin V-fluorescein isothiocyanate (5 μL), the cell suspension was kept in the dark for 10 min at room temperature. Next, after adding PI solution (10 μL), the suspension was stored in the dark for 5 min at room temperature. The cells were again washed twice with PBS and resuspended with annexin (300 μL). The percentages of dead cells and cells undergoing apoptosis were determined using a BD FACSCalibur flow cytometer (BD Biosciences, Franklin Lakes, NJ, USA). Annexin+/PI– was judged as early apoptosis and annexin+/PI+ as late apoptosis or death.

Cell-cycle perturbations induced by microbubbles with and without Fe_3O_4 nanoparticles after US treatment were analyzed by PI DNA staining. Briefly, exponentially growing 7721 cells were treated with 0.1, 0.5, and 0.75 W cm^{-2} US for 40 s each. At the end of each treatment, cells were collected after a gentle centrifugation at 1000 rpm for 5 min and then fixed in 70% ethanol for at least 2 h at 4 °C. Ethanol-suspended cells were diluted with PBS then centrifuged at 1000 rpm for 5 min to remove residual ethanol. For cell-cycle analysis, the cell samples were suspended in DNase-free Rnase (0.1 mL) and then the solution was incubated at 37 °C for 30 min. After adding PI solution (400 μL), the suspension was stored in the dark for 30 min at 4 °C. Cell-cycle profiles were studied by using a BD FACSCalibur flow cytometer (BD Biosciences, Franklin Lakes, NJ, USA). The data were statistically analyzed using the ModFit2.0 software.

Measurement of Intracellular Calcium Concentration: Fluorescence imaging and qualification of Ca^{2+} were performed using the indicator dye Fluo-3AM (Beyotime Institute of Biotechnology, China). After US exposure and treatment with NP-embedded and non-NP-embedded microbubbles, cells were separated from free microbubbles and fragments. Next, the cells were resuspended in the PBS solution (0.5 mL). The Fluo-3 Am (1 μM) was added into the solution and incubated for 30 min at 37 °C. After loading, the cells were washed three times with PBS. The Fluo-3-loaded cells can then be used for qualitative fluorescence imaging and quantitative flowcytometry measurement.[47,48] The optical observations and imaging were achieved by using the epifluorescent mode (excitation wavelength: 488 nm; fluorescence wavelength: 530 nm) of a microscope equipped with a digital Coolsnap MP3.3 camera (Axioskop 200, Carl Zeiss, Germany) and the mean fluorescence intensity of Ca^{2+} was obtained by using a BD FACSCalibur flow cytometer (BD Biosciences, Franklin Lakes, NJ, USA).

Statistical Analysis: Unless indicated otherwise, values are represented as the mean ± standard deviation (SD). For cell viability, cellular iron content, cell cycle, and Ca^{2+} level, direct comparisons between NP-embedded microbubbles and non-NP-embedded microbubbles were performed using the unpaired Student's t-test, and the statistical significance was assessed at $P < 0.05$ for all studies.

Acknowledgements

This investigation was financially funded by the National Important Science Research Program of China (Nos. 2006CB705602, 2011CB933500), National Natural Science Foundation of China (Nos. 60725101, 50872021, 31000453), and Research Fund of Young Teachers for the Doctoral Program of Higher Education of China (Nos. 20100092120038). We wish to extend our appreciation to Laboratory of Molecular Imaging, Department of Radiology, Zhongda Hospital, Southeast University for the kind help of the MRI experiments.

[1] N. T. K. Thanha, L.A.W. Greena, *Nano Today* **2010**, *5*, 213–230.
[2] W. Cai, X. Chen, *Small* **2007**, *3*, 1840–1854.
[3] M. A. Phillips, M. L. Gran, N. A. Peppas, *Nano Today* **2010**, *5*, 143–159.
[4] R. Landsiedel, L. Ma-Hock, A. Kroll, D. Hahn, J. Schnekenburger, K. Wiench, W. Wohlleben, *Adv. Mater.* **2010**, *22*, 2601–2627.
[5] J. H. Lee, M. V. Yigit, D. Mazumdar, Y. Lu, *Adv. Drug Delivery Rev.* **2010**, *62*, 592–605.
[6] R. A. Petros, J. M. DeSimone, *Nat. Rev. Drug Discov.* **2010**, *9*, 615–627.
[7] L. Zhang, S. Qiao, Y. Jin, H. Yang, S. Budihartono, F. Stahr, Z. Yan, X. Wang, Z. Hao, G. Q. Lu, *Adv. Funct. Mater.* **2008**, *18*, 3203–3212.
[8] L. Zhang, S. Z. Qiao, L. Cheng, Z. Yan, G. Q. Lu, *Nanotechnology* **2008**, *19*, 435608.
[9] L. Zhang, S. Z. Qiao, Y. G. Jin, Z. G. Chen, H. C. Gu, G. Q. Lu, *Adv. Mater.* **2008**, *20*, 805–809.
[10] V. P. Torchilin, *Adv. Drug Delivery Rev.* **2006**, *58*, 1532–1555.
[11] A. S. Diosa, M. E. Díaz-García, *Anal. Chim. Acta* **2010**, *666*, 1–22.
[12] A. Sandhu, H. Handa, M. Abe, *Nanotechnology* **2010**, *21*, 442001.
[13] H. Hong, Y. Yang, Y. Zhang, W. Cai, *Curr. Top. Med. Chem.* **2010**, *10*, 1237–1248.
[14] S. Ju, G. Teng, Y. Zhang, M. Ma, F. Chen, Y. Ni, *Magn. Reson. Imag.* **2006**, *24*, 611–617.
[15] C. Zhang, T. Liu, J. Gao, Y. Su, C. Shi, *Mini Rev. Med. Chem.* **2010**, *10*, 194–203.
[16] A. K. Gupta, M. Gupta, *Biomaterials* **2005**, *26*, 3995–4021.
[17] J. Chomoucka, J. Drbohlavova, D. Huska, V. Adam, R. Kizek, J. Hubalek, *Pharmacol. Res.* **2010**, *62*, 144–149.
[18] E. J. Akins, P. Dubey, *J. Nucl. Med.* **2008**, *49*, 180S-195S.
[19] S. Ganta, H. Devalapally, A. Shahiwala, M. Amiji, *J. Control. Release* **2008**, *126*, 187–204.
[20] T. Hoare, J. Santamaria, G. F. Goya, S. Irusta, D. Lin, S. Lau, R. Padera, R. Langer, D. S. Kohane, *Nano Lett.* **2009**, *9*, 3651–3657.
[21] M. Caldorera-Moore, N. A. Peppas, *Adv. Drug Delivery Rev.* **2009**, *61*, 1391–1401.

[22] A. L. Klibanov, *Investig. Radiol.* **2006**, *41*, 354–362.
[23] F. Cavalieri, M. Zhou, M. Ashokkumar, *Curr. Top. Med. Chem.* **2010**, *10*, 1198–1210.
[24] B. G. De Geest, A. G. Skirtach, A. A. Mamedov, A. A. Antipov, N. A. Kotov, S. C. De Smedt, G. B. Sukhorukov, *Small* **2007**, *3*, 804–808.
[25] G. D. Pangu, K. P. Davis, F. S. Bates, D. A. Hammer, *Macromol. Biosci.* **2010**, *10*, 546–554.
[26] J. Wu, W. L. Nyborg, *Adv. Drug Delivery Rev.* **2008**, *60*, 1103–1116.
[27] R. K. Schlicher, H. Radhakrishna, T. P. Tolentino, R. P. Apkarian, V. Zarnitsyn, M. R. Prausnitz, *Ultrasound Med. Biol.* **2006**, *32*, 915–924.
[28] J. C. Chappell, J. Song, C. W. Burke, A. L. Klibanov, R. J. Price, *Small* **2008**, *4*, 1769–1777.
[29] L. J. M. Juffermans, A. van Dijk, C. A. M. Jongenelen, B. Drukarach, A. Reijerkerk, H. E. de Vries, O. Kamp, R. J. P. Musters, *Ultrasound Med. Biol.* **2009**, *35*, 1917–1927.
[30] H. Ke, Z. Xing, B. Zhao, J. Wang, J. Liu, C. Guo, X. Yue, S. Liu, Z. Tang, Z. Dai, *Nanotechnology* **2009**, *20*, 425105.
[31] M. H. Lee, V. Prasad, D. Lee, *Langmuir* **2010**, *26*, 2227–2230.
[32] Z. P. Chen, R. Z. Xu, Y. Zhang, N. Gu, *Nanoscale Res. Lett.* **2009**, *4*, 204–209.
[33] L. J. M. Juffermans, O. Kamp, P. A. Dijkmans, C. A. Visser, R. J. P. Musters, *Ultrasound Med. Biol.* **2008**, *34*, 502–508.
[34] F. E. Schweizer, T. A. Ryan, *Curr. Opin. Neurobiol.* **2006**, *16*, 298–304.
[35] P. L. McNeil, R. A. Steinhardt, *Annu. Rev. Cell Dev. Biol.* **2003**, *19*, 696–731.
[36] J. Wu, *Progr. Biophys. Mol. Biol.* **2006**, *93*, 363–373.
[37] F. Yang, N. Gu, D. Chen, X. Xi, D. Zhang, Y. Li, J. Wu, *J. Control. Release* **2008**, *131*, 205–210.
[38] Z. Fan, R. E. Kumon, J. Park, C. X. Deng, *J. Control. Release* **2010**, *142*, 31–39.
[39] Y. Zhou, J. Shi, J. Cui, C. X. Deng, *J. Control. Release* **2008**, *126*, 34–43.
[40] S. Orrenius, B. Zhivotovsky, P. Nicotera, *Nat. Rev. Mol. Cell Biol.* **2003**, *4*, 552–565.
[41] H. L. Roderick, S. J. Cook, *Nat. Rev. Cancer* **2008**, *8*, 361–375.
[42] D. G. Shchukin, D. A. Gorin, H. Möhwald, *Langmuir* **2006**, *22*, 7400–7404.
[43] T. F. Massoud, S. S. Gambhir, *Gene. Dev.* **2003**, *17*, 545–580.
[44] R. Weissleder, M. J. Pittet, *Nature* **2008**, *452*, 580–589.
[45] F. Yang, Y. Li, Z. Chen, Y. Zhang, J. Wu, N. Gu, *Biomaterials* **2009**, *30*, 3882–3890.
[46] F. Blanc-Béguina, S. Nabilyb, J. Gieraltowskib, A. Turzoc, S. Querellouc, P. Y. Salaunc, *J. Magn. Magn. Mater.* **2009**, *321*, 192–197.
[47] S. Orrenius, B. Zhivotovsky, P. Nicotera, *Nat. Rev. Mol. Cell Biol.* **2003**, *4*, 552–565.
[48] H. L. Roderick, S. J. Cook, *Nat. Rev. Cancer* **2008**, *8*, 361–375.

Received: December 15, 2010
Revised: January 7, 2011
Published online: February 25, 2011